



RESEARCH ARTICLE

10.1029/2019GB006336

Key Points:

- Quantification of redistribution of DIC by ocean meridional circulation is related to physical and biological processes
- Transports of solubility carbon dominates the upper ocean and the NADW, biogenic carbon the deep ocean
- Pacific biological pump is the most important process retaining carbon on longer time scales

Supporting Information:

- Supporting Information S1

Correspondence to:

A. Aldama-Campino,
aitor.aldama@outlook.com

Citation:

Aldama-Campino, A., Fransner, F., Ödalen, M., Groeskamp, S., Yool, A., Döös, K., & Nycander, J. (2020). Meridional ocean carbon transport. *Global Biogeochemical Cycles*, 34, e2019GB006336. <https://doi.org/10.1029/2019GB006336>

Received 26 JUN 2019

Accepted 3 JUN 2020

Accepted article online 7 JUL 2020

Meridional Ocean Carbon Transport

Aitor Aldama-Campino^{1,2} , Filippa Fransner³ , Malin Ödalen^{1,2,4} , Sjoerd Groeskamp⁵ , Andrew Yool⁶ , Kristofer Döös^{1,2} , and Jonas Nycander^{1,2}

¹Department of Meteorology, Stockholm University, Stockholm, Sweden, ²Bolin Centre for Climate Research, Stockholm University, Stockholm, Sweden, ³Geophysical Institute, University of Bergen, and Bjerknes Centre for Climate Research, Bergen, Norway, ⁴Department of Geosciences, University of Arizona, Tucson, AZ, USA, ⁵NIOZ Royal Netherlands Institute for Sea Research, Department of Ocean Systems, and Utrecht University, Texel, The Netherlands, ⁶National Oceanography Centre, Southampton, UK

Abstract The ocean's ability to take up and store CO₂ is a key factor for understanding past and future climate variability. However, qualitative and quantitative understanding of surface-to-interior pathways, and how the ocean circulation affects the CO₂ uptake, is limited. Consequently, how changes in ocean circulation may influence carbon uptake and storage and therefore the future climate remains ambiguous. Here we quantify the roles played by ocean circulation and various water masses in the meridional redistribution of carbon. We do so by calculating streamfunctions defined in dissolved inorganic carbon (DIC) and latitude coordinates, using output from a coupled biogeochemical-physical model. By further separating DIC into components originating from the solubility pump and a residual including the biological pump, air-sea disequilibrium, and anthropogenic CO₂, we are able to distinguish the dominant pathways of how carbon enters particular water masses. With this new tool, we show that the largest meridional carbon transport occurs in a pole-to-equator transport in the subtropical gyres in the upper ocean. We are able to show that this pole-to-equator DIC transport and the Atlantic meridional overturning circulation (AMOC)-related DIC transport are mainly driven by the solubility pump. By contrast, the DIC transport associated with deep circulation, including that in Antarctic bottom water and Pacific deep water, is mostly driven by the biological pump. As these two pumps, as well as ocean circulation, are widely expected to be impacted by anthropogenic changes, these findings have implications for the future role of the ocean as a climate-buffering carbon reservoir.

1. Introduction

The ocean circulation and its redistribution of carbon are important parts of the global carbon cycle and have significant impacts on the atmospheric pCO₂ (Ciais et al., 2013; Mikaloff Fletcher et al., 2007; Sabine et al., 2004; Sarmiento & Gruber, 2006). With rising atmospheric pCO₂ and related climate change, many studies have focused on air-sea CO₂ exchange (e.g., Landschützer et al., 2015; Le Quéré et al., 2007; Takahashi et al., 2002; Yasunaka et al., 2018) and how the physical and biological pumps drive the air-sea exchange (Volk & Hoffert, 2013). How this air-sea CO₂ exchange connects the surface to the ocean interior via large scale ocean circulation is, however, less well constrained (Levy et al., 2013). This is largely related to the difficulties in distinguishing the role of ocean water masses and circulation patterns in ocean carbon transport.

Estimates of meridional ocean carbon transport have been made through inverse calculations based on observed air-sea CO₂ exchange and its variations (Gloor et al., 2003; Gruber et al., 2009; Mikaloff Fletcher et al., 2007). These do not, however, give any information on the control that the various circulation cells exerts on carbon transport and redistribution within the ocean. Meridional carbon transport has also been calculated by the product of volume flow and carbon concentrations (Brewer et al., 1989; Broecker & Peng, 1992), which gives a rough estimate, but does not give a global view. Iudicone et al. (2011) made a detailed analysis of the role of separate water masses in the transports of carbon in and out of the Southern Ocean. Studies such as these provide an important basis for our knowledge of overall ocean carbon transports. However, they do not explain how the transport is connected globally, nor do they clarify the sources of the transported carbon, that is, whether it originates from the physical or the biological pumps.

©2020. The Authors.

This is an open access article under the terms of the Creative Commons Attribution License, which permits use, distribution and reproduction in any medium, provided the original work is properly cited.

The physical—or solubility—pump is the mechanism by which carbon enters the deep ocean via sites of deep water formation (Volk & Hoffert, 1985). These sites transfer dense seawater into the ocean interior, typically at high latitudes, where cooler surface temperatures enhance the solubility of CO_2 . Consequently, waters reaching the ocean interior have elevated concentrations of dissolved inorganic carbon (DIC) driven by this physical mechanism. In contrast, the biological pump is ultimately driven by the production of organic matter (plus carbonate biominerals) by photosynthetic phytoplankton at the ocean's surface (Volk & Hoffert, 1985). After processing through the foodweb, a fraction of this production is exported from the surface to the interior ocean by either gravitational sinking or subduction. Its remineralization within the ocean liberates DIC, elevating water column concentrations through biological mechanisms.

The aim of this study is to present a diagnostic tool to estimate the global meridional transport of DIC related to ocean circulation cells in the ocean interior. It builds on Groeskamp et al. (2016), who developed a new method for calculating the transport of anthropogenic carbon to the ocean interior based on streamfunctions. Further, we link the origins of the transported carbon to the physical and biological ocean carbon pumps, which comprise the main pathways by which carbon enters the ocean interior. By doing this, we provide further clues to understanding the role of physical and biological ocean processes in ocean carbon storage and, by inference, in regulating atmospheric pCO_2 . This method, which consists of a dimensional reduction of the system to a two dimensional projection, can be used for instance to simplify model intercomparisons or to identify notable changes in ocean carbon transport and identify the responsible processes.

2. Methods

2.1. Carbon Decomposition

In the ocean, dissolved CO_2 exists in several different forms. About 90% exists as bicarbonate, 9% as carbonate, and a small fraction of the concentration is in the form of aqueous CO_2 and carbonic acid (Williams & Follows, 2011). Together, these species are commonly known as DIC. The total ocean concentration of DIC will from now on be referred to as C_{tot} . Per Equation 1, it can be partitioned into contributions from different processes associated with the solubility pump and the biological pump (Eggleston & Galbraith, 2018; Ito & Follows, 2005; Ödalen et al., 2018; Williams & Follows, 2011). The partitioning allows us to quantify the contribution of solubility pump and biological pump processes to carbon transports in different water masses.

The solubility pump describes the pathway for carbon that enters the ocean via physico-chemical dissolution in the surface ocean. In our simulations, this consists of three components: saturation carbon (C_{sat}), disequilibrium carbon (C_{dis}), and anthropogenic carbon (C_{anth}). In this paper, we focus mainly on C_{sat} , which is described in more detail below. The biological pump involves carbon that is biologically fixed in particulate material in the surface ocean and then transported (via gravitational sinking and circulation) to the deep ocean where it is remineralized back to DIC. We refer to this DIC as C_{bio} .

We apply the same ocean carbon partitioning framework as in Lauderdale et al. (2013), with the addition of a component associated with anthropogenic emissions (Couldrey, 2018):

$$C_{\text{tot}} = C_{\text{sat}} + C_{\text{bio}} + \underbrace{C_{\text{dis}} + C_{\text{anth}}}_{C_{\text{res}}} + \epsilon. \quad (1)$$

Here, the ϵ term represents any discrepancies associated with the computation methods in the solution of the carbon system equations (Lewis et al., 1998) and the computation of C_{bio} and its constituents (McDougall & Barker, 2011; Lauderdale et al., 2013; see the Supporting Information).

C_{sat} , the bulk of C_{tot} associated with the solubility pump, originates from CO_2 dissolving in water until the water reaches saturation, for a constant reference atmospheric pCO_2 (henceforth $\text{pCO}_2^{\text{atm}}$), at the ambient ocean temperature, alkalinity, and salinity (see section 2.3). Whenever water is not at saturation when it leaves the ocean surface, there is also a disequilibrium contribution to carbon (C_{dis}), which can be positive or negative. If $\text{pCO}_2^{\text{atm}}$ changes over time, for example, through anthropogenic emissions, this contribution to ocean C_{tot} can be accounted for separately (C_{anth}) (Couldrey, 2018). In this work, however, we do not study the separate contributions from C_{dis} and C_{anth} , so together with ϵ , these are treated as a solubility pump residual (C_{res} ; see Equation 1).

C_{sat} , C_{dis} , and C_{anth} are so-called preformed tracers, which are only modified at the ocean surface and act as passive tracers in the ocean interior. C_{bio} is equal to zero at the surface, but has local sources in the interior ocean. As C_{sat} acts as a conserved tracer in the interior ocean, we choose to study it separately. We also look at the remaining terms taken together ($C_{bio+res}$) by subtracting the computed C_{sat} from C_{tot} :

$$C_{tot} - C_{sat} = C_{bio+res}. \quad (2)$$

2.2. Meridional Streamfunctions

2.2.1. Meridional Overturning Streamfunctions

Streamfunctions are a diagnostic tool often used in both atmospheric science and physical oceanography, which help to understand different processes such as volume transports. The idea behind streamfunctions is a dimensional reduction of the system to a two-dimensional projection. The most traditional streamfunctions are based on two geographical coordinates. For instance, the latitude-depth stream function $\Psi(\phi_0, z_0)$, usually referred to as the meridional overturning stream function is, among the different set of streamfunctions, the most used and known one. The meridional overturning streamfunction is given by the following equation:

$$\Psi(\phi_0, z_0) = \frac{1}{t_f - t_0} \int_{t_0}^{t_f} \int_{\Omega} \delta[\phi_0 - \phi] \mu[z_0 - z] v(\vec{x}, t) d\Omega dt, \quad (3)$$

where ϕ_0 is the chosen latitude, z_0 is the reference depth, $v(\vec{x}, t)$ is the meridional velocity field (in m s^{-1}), t_f and t_0 represent the final and the initial time respectively (in s), and Ω represents the volume domain over which the streamfunction is computed. In this particular case, where we are defining latitude ϕ to describe the meridional coordinate, $d\Omega$ has area units (m^2) and is given by $d\Omega = d\phi dx dz$. The units of the streamfunction are given in $[\text{m}^3 \text{s}^{-1}]$ (which represent a volume transport). For convenience, however, the results will be presented in Sverdrups, $1 \text{ Sv} \equiv 10^6 \text{ m}^3 \text{s}^{-1}$.

By imposing both the Dirac delta pseudo-function $\delta[\star]$ and the Heaviside step function $\mu[\star]$, the stream function only considers the volume fluxes at ϕ_0 at depths equal or below z_0 . Therefore, this stream function represents the total average meridional mass transport below a given depth value z_0 , at a chosen latitude ϕ_0 . If there are no mass sources or sinks, this value also represents the total vertical mass transport north of ϕ_0 at a depth z_0 .

2.2.2. A Generalized Meridional Streamfunction

The meridional overturning circulation can be generalized to any coordinate ξ which could be another geographical coordinate (e.g., longitude as in the barotropic stream function), a thermodynamic coordinate (e.g., temperature), or as we will present in this work a biogeochemical tracer. The generalized meridional streamfunctions is described by the following equation:

$$\Psi(\phi_0, \xi_0) = \frac{1}{t_f - t_0} \int_{t_0}^{t_f} \int_{\Omega} \delta[\phi_0 - \phi] \mu[\xi_0 - \xi(\vec{x}, t)] v(\vec{x}, t) d\Omega dt, \quad (4)$$

where ξ_0 is the reference isoline value of the selected tracer (in this study C_{tot} and C_{sat}). A positive value of the streamfunction represents a net northward volume transport for waters with a tracer value lower or equal to ξ_0 .

There is a special set of streamfunctions where a proper choice of the coordinate ξ transforms the general meridional stream function into an extended version of the meridional overturning circulation. In this case, ξ , a nongeographical coordinate, behaves as a pseudo-depth where its values can be related to a depth level. This relation facilitates an estimate of the vertical position in the geographical space directly from the streamfunction in the $\phi - \xi$ space. Nevertheless, it is possible to identify the overturning cells that may arise from $\Psi(\phi, \xi)$ in geographical space by locating them for a given latitude and tracer value.

Moreover, the streamfunction can be computed for a particular basin by applying a mask function to the integral. In this study, we have considered three basins: the Southern Ocean (covering all the water masses south of cape Agulhas, 34°S), the Atlantic Ocean (which includes the Mediterranean and Black Sea, and the Arctic Ocean), and the Indo-Pacific Ocean. Cape Agulhas is selected as the cut-off latitude to avoid splitting the Antarctic circumpolar current (ACC) into two different basins. However, this split cannot be applied to the tracer coordinate. For example, it is not possible to compute the associated streamfunction for $C_{bio+res}$ by subtracting the C_{sat} streamfunction from the C_{tot} streamfunction. This is a result of the nonlinearity of the step function inside the integral.

2.2.3. Meridional Transports

In a nondivergent fluid, the meridional transport of the tracer can be computed by integrating the streamfunction along the tracer space. However, the ocean is a divergent fluid as the evaporation, precipitation, and river runoff act as sources or sinks at the surface. In order to minimize the effect of the divergence, we will introduce a reference tracer value ξ^R . The transport is given by

$$Tr(\phi_0) = \int_{\xi_{min}}^{\xi_{max}} (\xi_0 - \xi^R) \frac{\partial \Psi(\phi_0, \xi_0)}{\partial \xi_0} d\xi_0. \quad (5)$$

In this study, we chose the mean value of the tracer as ξ^R . The sensitivity to the choice of the reference value is discussed in Appendix B. Inserting the definition of the streamfunction, we will obtain the following result:

$$\begin{aligned} Tr(\phi_0) &= \int_{\xi_{min}}^{\xi_{max}} (\xi_0 - \xi^R) \left(\frac{1}{t_f - t_0} \int_{t_0}^{t_f} \int_{\Omega} \delta[\phi_0 - \phi] \delta[\xi_0 - \xi(\vec{x}, t)] v(\vec{x}, t) d\Omega dt \right) d\xi_0 = \\ &= \frac{1}{t_f - t_0} \int_{t_0}^{t_f} \int_{\Omega} \delta[\phi_0 - \phi] \left(\int_{\xi_{min}}^{\xi_{max}} (\xi_0 - \xi^R) \delta[\xi_0 - \xi(\vec{x}, t)] d\xi_0 \right) v(\vec{x}, t) d\Omega dt \\ &= \frac{1}{t_f - t_0} \int_{t_0}^{t_f} \int_{\Omega} \delta[\phi_0 - \phi] (\xi(\vec{x}, t) - \xi^R) v(\vec{x}, t) d\Omega dt. \end{aligned} \quad (6)$$

This recovers the traditional expression for a meridional transport of a tracer computed directly from the velocity and the tracer field. Most of the fields analyzed in this study (C_{tot} , C_{sat} , and $C_{bio+res}$) are positive definite; therefore, a positive value of the transport represents a northward transport of the tracer. A description on how to compute the streamfunction and the transports numerically can be found in Appendices A1 and B1.

2.3. Model Data and Analysis

We use the output from a simulation of the coupled physical-biogeochemical model NEMO-MEDUSA (Yool et al., 2015). NEMO (Madec, 2012) is used here in a global ORCA025 configuration, with a horizontal resolution of approximately 0.25° (an average grid cell size of 19.0 km globally) and with 75 vertical levels (increasing in thickness from 1 m at the surface to 200 m at 6,000 m). This particular simulation has been run using NEMO v3.4 with the LIM2 sea-ice model (Timmermann et al., 2005).

The biogeochemical model, MEDUSA-2 (Yool et al., 2013), is an intermediate complexity framework containing a representation of the elemental cycles of nitrogen, carbon, oxygen, silicon, and iron. The plankton ecosystem is composed of dual size classes of phytoplankton, zooplankton, and detritus components. It is a nitrogen-based model, with the biological transformations of other elemental cycles related to that of nitrogen by fixed “Redfield” ratios (except silicon, which has a dynamic ratio).

The output used here is a 10-year period from 2000 to 2009, drawn from a run that contains both historical and future simulations, as it is run for the period 1975–2099 (Yool et al., 2015). The model was initialized in 1975 using physical and biogeochemical fields from a lower horizontal resolution simulation (ORCA1; 1° horizontal resolution), run for the period 1860–1975. This lower-resolution model was forced at its surface boundary using atmospheric fields (including atmospheric pCO_2) from a CMIP5 historical simulation of the HadGEM2-ES model (Jones et al., 2011; Yool et al., 2015). The ORCA025 configuration continued with the same forcing regime from 1975 onwards. After 2005, the simulation followed an IPCC climate projection using the Representative Concentration Pathway (RCP) 8.5 scenario. This future projection describes a continuous increase of greenhouse gas emission throughout the 21st century reaching a radiative forcing of 8.5 W m^{-2} by the end of the century.

The saturation carbon, C_{sat} , was computed using the carbon system equations solver CO2SYS (Lewis et al., 1998) by providing in situ temperature, salinity, global mean alkalinity, and a reference pCO_2^{atm} based on the 1860 value (286 ppm). The climatological cross sections of C_{tot} in the Atlantic (25°W) and Indo-Pacific (170°W) are computed from the model output of the selected ten year time period (2000–2009; Figure 1). This climatology is computed from the model output of the selected 10-year time period (2000–2009). In panels c and d, we show the corresponding computed C_{sat} . Notice that while C_{sat} increases monotonically with depth, we can find local maxima of C_{tot} in the interior ocean. This makes C_{sat} an ideal tracer for interpretation of streamfunctions as it allows us to allocate values of Ψ to a given depth.

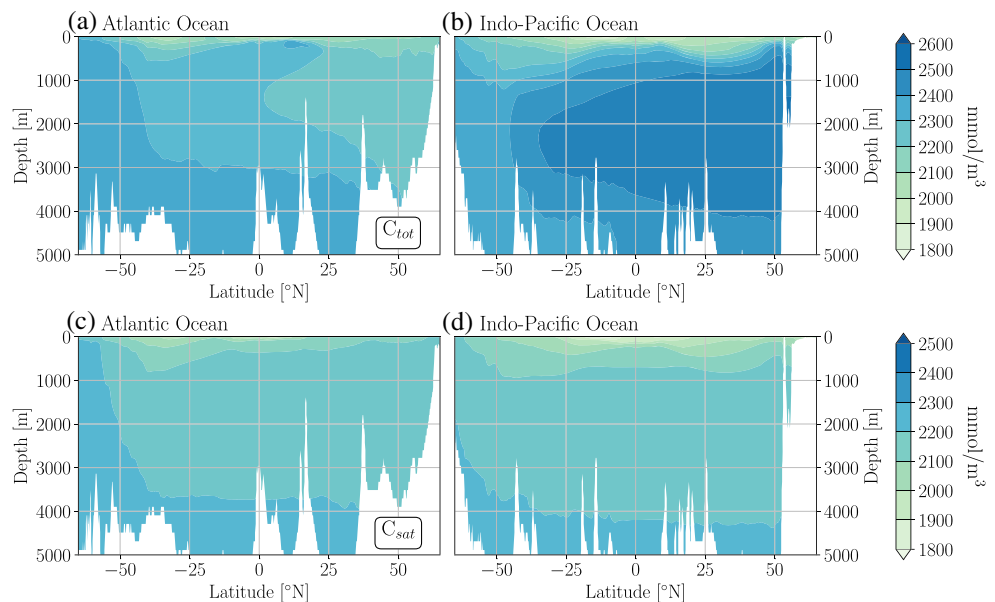


Figure 1. Climatological cross sections for C_{tot} (upper row) and for C_{sat} (lower row) computed from the model output of the selected 10-year time period (2000–2009). Panels (a) and (c) show the Atlantic Ocean (25°W), and panels (b) and (d) show the Indo-Pacific Ocean (170°W).

3. Results and Discussion

In the following sections, we present first the latitude-depth streamfunction to help the reader with the following discussions of the latitude-carbon streamfunction (section 3.1). Next, we introduce and discuss the results of the carbon-latitude streamfunction (section 3.2). The role of different water masses and the geographical identification of the cells are further discussed in section 3.3. We first examine the C_{tot} -latitude streamfunction for the Atlantic and Indo-Pacific oceans to better understand the underlying mechanisms of their cells and related role in the ocean carbon cycle. This simplifies the identification of different water masses. Thereafter, we separate the associated carbon transports to each of the cells to quantify their contribution to the total carbon transport (section 3.4). Finally, the roles of the physical and biological pumps in the meridional carbon transport are discussed (section 3.5).

3.1. The Meridional Overturning Streamfunction

The meridional overturning streamfunction shows the different circulation patterns in the Atlantic Ocean (Figure 2a) and in the Indo-Pacific (Figure 2b). The Southern Ocean has not been split to avoid anomalous results of the streamfunction in the ACC region.

The Atlantic Ocean is characterized by two main cells: a clockwise overturning cell (A1) located above 3,000 m and spanning along all the latitudes in the basin, and anticlockwise overturning cell (A2) located at the bottom of the basin. The former describes the northward transport of warm surface waters, their sinking at high latitudes as a result of a buoyancy loss, and the southward return flow at deeper levels. This cell is linked to the Atlantic meridional overturning circulation (AMOC). The latter can be linked to the Antarctic bottom water (AABW) which is formed around Antarctica and is the most common water mass found at the bottom of the ocean (Talley, 2013).

The Indo-Pacific ocean is characterized by three main cells: two almost symmetric cells near the surface (IP1 and IP2), and a third cell that covers almost the entire basin (IP3). The shallow but strong cells are a result of the wind-driven circulation in the tropics. The spinning of these overturning cells describes a divergence at the surface due to the Ekman transport and a convergence of waters at the equator in deeper levels (≈ 500 m) which leads to an upwelling in the region. Cell IP3 captures the Pacific deep water (PDW) and the AABW in the region. This cell describes a northward volume transport at the bottom and a southward volume transport at intermediate depths. Note that the strongest values are located in the Southern Hemisphere. The value of $\Psi(\phi, z)$ in the North Pacific is very low due to the slow circulation in the region (Talley, 2013).

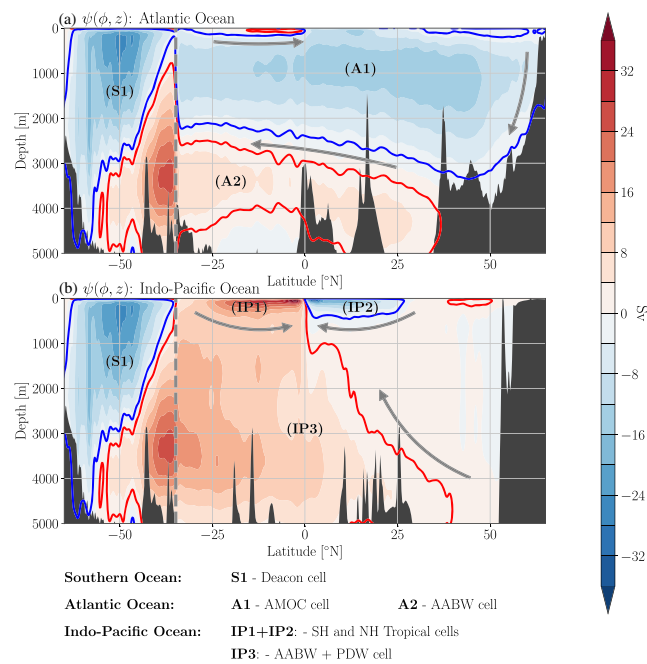


Figure 2. The meridional overturning streamfunction in latitude-depth space for the Atlantic Ocean (top) and the Indo-Pacific Ocean (bottom). The red (blue) cells describes counterclockwise (clockwise) circulations. The circulation of the overturning cells is given by the gray arrows. The gray dash line represents the cape Agulhas latitude.

Finally, the Southern Ocean is characterized by a strong and deep overturning cell (S1). This cell is known as the Deacon cell and captures most of the southward Ekman return flow in the Southern Ocean. As shown by Döös and Webb (1994), this is an artifact of projecting the volume fluxes in the latitude-depth space. The Deacon cells disappear if the meridional volume fluxes are projected into the latitude-neutral density space instead.

Many of the cells that appear in $\Psi(\phi, z)$ will have an analogous overturning cell in the latitude-carbon streamfunctions that we introduce in the coming sections.

3.2. The Latitude-Carbon Streamfunction

The calculated global carbon-latitude streamfunction and its different circulation cells are shown in Figure 3a. High C_{tot} concentrations are associated with polar waters (due to higher gas solubility in colder water, e.g., Raven & Falkowski, 1999; Volk & Hoffert, 2013; Weiss, 1974) and deep waters (due to the biological pump, e.g., Broecker, 1983; Volk & Hoffert, 2013). For visualization purposes, and in order to have near-surface circulation cells above those associated with deep waters, the y-axis has been reversed. Note that in the Indo-Pacific the highest concentrations are located at about 2,000-m depth, making the interpretation of the streamfunction in this region a bit harder, which will be discussed in the next section. To illustrate the location of surface waters in relation to the circulation cells, we have plotted the volume weighted zonal mean surface C_{tot} concentration (dashed black line).

The global streamfunction is characterized by five main circulation cells. The largest two surface cells are located between the equator and 40°N/S at relatively low C_{tot} concentrations (2,000–2,200 mmol m⁻³) and are strongly linked to the big wind-driven subtropical gyres, as will be shown in section 3.3. The cells are spinning in opposite directions, with the northern cell spinning clockwise (blue cell) and the southern one anticlockwise (red cell). These cells transport surface waters with low C_{tot} concentrations poleward and waters with higher C_{tot} concentrations equatorward. The increase in C_{tot} concentrations in the upper limb of these cells shows that there is a continuous uptake of atmospheric CO₂ in surface waters on their way poleward. In addition, another near-surface cell is observed in the Southern Ocean between 40°S and 60°S, with C_{tot} concentrations of 2,100–2,300 mmol m⁻³, and spinning clockwise. The upper limb of this cell is losing C_{tot} on its way northward. This cell can be linked to the activity of the ACC. The other two main cells

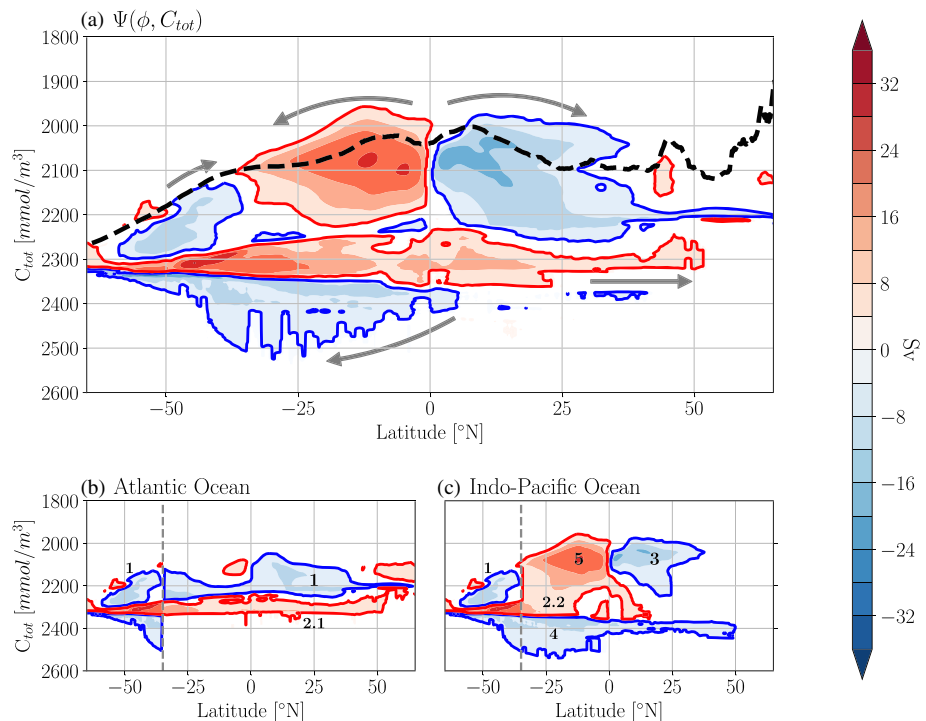


Figure 3. Upper panel: the global C_{tot} -latitude streamfunction. Note that the C_{tot} axes has been reversed. The red (blue) cells describe counterclockwise (clockwise) circulations. The volume weighted zonal mean surface concentration of C_{tot} is shown by the dashed black line. The lower panels represent the split of the global streamfunction into the Atlantic basin (which includes the Arctic Ocean) and the Indo-Pacific Ocean. The numbers represent the main cells of the streamfunction. The gray dashed line represents the cape Agulhas latitude.

occur with higher C_{tot} concentrations (2,200–2,500 mmol m^{-3}), span whole ocean basins (i.e., stretching across the equator), and represent deep and bottom waters.

3.3. The Role of the Cells

The global streamfunction $\Psi(\phi, \xi)$ is a composite of different cells which represent different processes and water masses. We therefore analyze the streamfunction for the two main ocean basins: the Atlantic and the Indo-Pacific Ocean, separately. In this study, we define a cell as being enclosed by the 4-Sv streamline. The identification of the main cells in the geographical (latitude-depth) space are shown in Figures 4a and 4b. The contours in these figures represent the fraction of volume at a given latitude and depth contained in the selected cell. The contours have been filled using a gradient color-map where darker colors represent higher fractions.

The Atlantic basin is characterized by two main cells spanning over the entire basin (Figure 3b). The first one (referred to as Cell 1) is bounded between C_{tot} concentrations between 2,000 and 2,250 mmol m^{-3} , spinning clockwise, and therefore transports surface waters with low C_{tot} concentration northward, and waters with higher C_{tot} concentration southward. The reprojection of this cell into geographical space (blue shading, in Figure 4a) shows that the majority of the cell is located at depths shallower than 1,000 m, except in the midlatitudes in the Northern Hemisphere where these waters can be located at almost 3,000 m. This cell and its transports can be associated with the AMOC, including the upper limb of the North Atlantic deep water (NADW), the tropical cell of the Northern Hemisphere, and the Agulhas leakage (Talley, 2013). The NADW extends as a narrow blue feature stretching from $\sim 40^\circ\text{N}$ to $>60^\circ\text{S}$ at a C_{tot} concentration of 2,200 mmol m^{-3} (see Figures 1 and 3b). At $>60^\circ\text{S}$, associated with the wind-driven upwelling, or the divergence zone, in the Southern Ocean (Marshall & Speer, 2012), the lower limb of this cell reaches surface waters and then continues northward with the Ekman transport. Note that the southern tropical cell is represented by the small and weak anticlockwise cell between 20°S and the equator; however, its contribution is very small. The second major cell (Cell 2.1), circulating anticlockwise, spreads at narrower C_{tot} concentrations confined around 2,300 mmol/m^3 . It transports waters with higher C_{tot} concentration northward, and lower

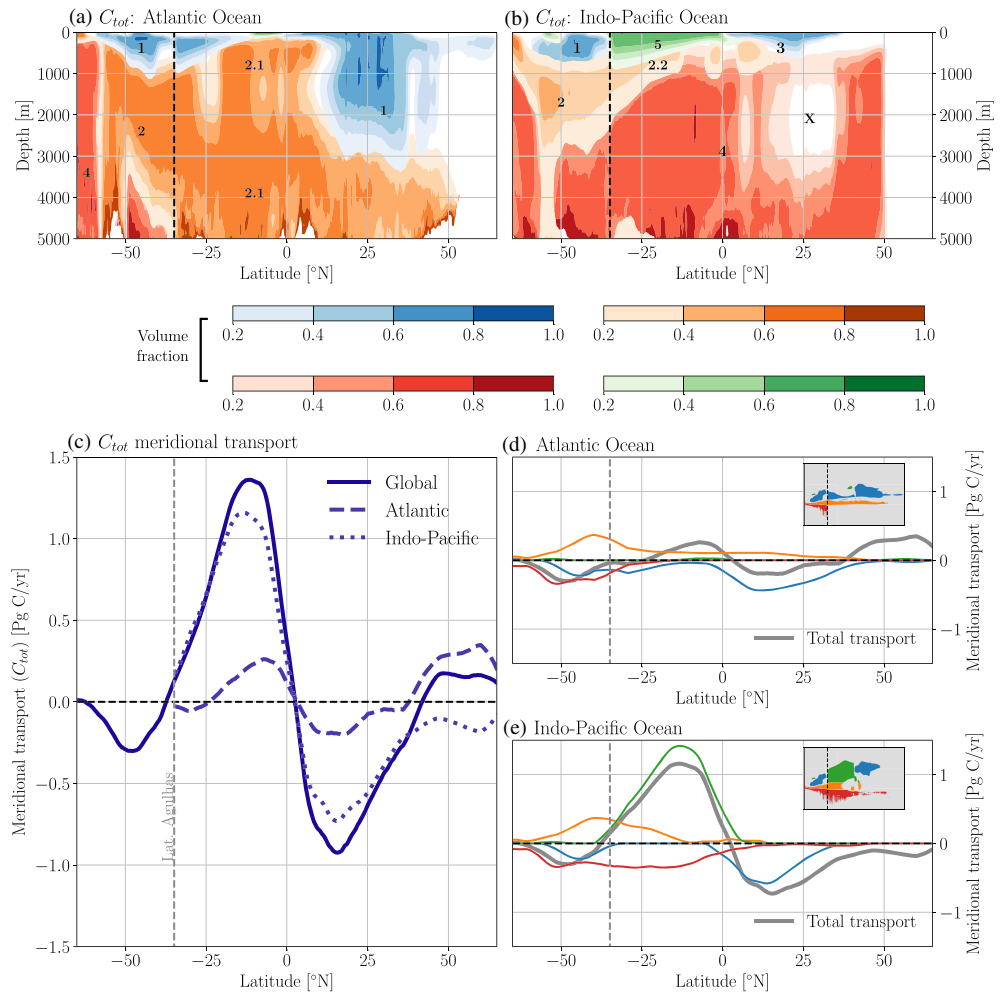


Figure 4. The identification of different cells (identified by numbers 1–5) for $\Psi(\phi, C_{tot})$ in geographical space for the Atlantic (a) and the Indo-Pacific (b) basins. The contours represent the fraction of volume at a given latitude and depth contained in the selected cell. Darker colors indicate higher fractions. (c) The global meridional transport of C_{tot} and the contribution of each of the cells in $\Psi(\phi, C_{tot})$ to the meridional transport for the Atlantic (d) and the Indo-Pacific basin (e). Each of the cells has an assigned color which is used for both the transport and the reprojection plots. The transports for the cells have been computed using a threshold of 4 Sv.

C_{tot} concentrations southward. The reprojection into the geographical space (orange shading in Figure 4) shows that the water masses described by this cell are located at intermediate and deeper levels, and therefore can be associated with intermediate waters, AABW, and the lower limb of NADW that upwells in the Southern Ocean (Talley, 2013).

In the Indo-Pacific Ocean, three distinct cells are observed. Near the surface, we find two cells of similar strength and shape, and opposite sign (Cells 3 and 5). These cells span from the equator up to the midlatitudes and cover concentrations between 2,000 and 2,200 mmol m^{-3} and contain the stronger circulation in this framework, up to 30 Sv. The water masses contained in these two cells are located above 1,000-m depth (green and blue shading) and represent the wind driven gyre circulation at the tropical Indo-Pacific Ocean. Similar to what we observed in the Atlantic Ocean, Cell 2.2 represents the intrusion of intermediate waters from the Southern Ocean into the Indo-Pacific basin. However, in contrast to the 2.1 cell in the Atlantic, this cell does not capture the bottom waters, which in the Indo-Pacific instead are captured by Cell 4. Cell 4 is spinning clockwise (see Figure 3) and is located at the highest C_{tot} concentrations observed (above 2,300 mmol m^{-3}). The water masses contained in this cell (shaded in red) can be found at any depths larger than 1,000 m in the Indo-Pacific Ocean, containing the northward flowing AABW and southward flowing PDW (Talley, 2013). The clockwise circulation of this cell means that there is a net southward transport of C_{tot} and

consequently that the C_{tot} transport is larger in the PDW than in the AABW. This comes as a result of the higher C_{tot} concentrations at mid-depth in the Pacific (Figure 1).

The empty area (marked with an X) between 20°N and 40°N and a mean depth of 2,000 m can be related to a region of slow or even stagnant waters that contribute with small volume transports below our selected threshold of 4 Sv. This is coined the shadow zone (de Lavergne et al., 2017). The sluggishness of these waters becomes apparent when observing that they coincide with the oxygen minimum and the C_{tot} maximum zone in the North Pacific Ocean (Figure S1 in the supporting information). Note that the C_{tot} maximum zone is not located at the bottom of the basin (as it is the case for the Atlantic and the Southern Ocean), confounding the use of C_{tot} as a pseudo-depth.

3.4. Associated Carbon Transports

The global transport of C_{tot} (Figure 4c) is described by a convergence of carbon at the equator and a divergence region at around 30°S. The maximum carbon transports are observed in the tropics around 20°N/S with a maximum northward C_{tot} transport of 1.4 Pg C yr⁻¹ in the Southern Hemisphere and a maximum southward transport of 0.9 Pg C yr⁻¹ in the Northern Hemisphere (Figure 4c). The carbon transport convergence is a result of the strong surface tropical cells that transport carbon equatorward where it is outgassed to the atmosphere because of the low solubility in the warm tropical water. The divergence of C_{tot} at about 30°S in the Southern Ocean is mainly caused by the net southward transport of Cell 1 and the net northward transport of Cell 5. It is associated with the Southern Ocean subduction zone, where northward flowing surface waters of the Southern Ocean is subducted below warmer subtropical waters (Speer et al., 2000).

The global signal is mainly dominated by the transports in the Indo-Pacific Ocean. Different factors are responsible for this: the width of the basin, the higher concentrations of C_{tot} in the Indo-Pacific, and the role of the surface tropical cells. The cells contribute in different ways to the C_{tot} transport as they represent different dynamical and/or biogeochemical processes (see Figure 4e). Both Cell 5 (green) and Cell 3 (blue) are the largest contributors to the meridional transport in the Indo-Pacific Ocean, and also on a global scale, with C_{tot} transports amounting to 1.42 and -0.58 Pg C yr⁻¹, respectively. The larger absolute transport in Cell 5 compared to Cell 3 can, to a large extent, be explained by the wider southern part of the Indo-Pacific. As mentioned in the previous section, these tropical cells represent the near-surface wind driven tropical circulation. A combination of the strong dynamical cells and the upwelling of carbon rich waters from deeper waters results in a strong equatorward transport in the tropics. The tropical cells are described in temperature-salinity coordinates by Döös et al. (2012), Zika et al. (2012), and Groeskamp et al. (2014) and in latitude-density coordinates by Ballarotta et al. (2014). Cell 4, which consist of AABW and PDW, has a net southward transport of carbon, amounting to -0.35 Pg C yr⁻¹. This substantial carbon transport is a result of the high concentrations of C_{tot} which compensates the small volume fluxes in the deeper layers.

The Atlantic basin contributes with much weaker transports (Figure 4d). The Atlantic meridional transport of carbon is the result of a compensation between the southward C_{tot} transport driven by Cell 1 (amounting to -0.44 Pg C yr⁻¹) and the northward transport driven by C_{tot} rich waters in the AABW in Cell 2.1 (up to 0.37 Pg C yr⁻¹). It is important to note that Cell 1 not only includes the NADW but also includes the tropical cell of the North Atlantic. There is a small convergence at the equatorial regions driven by the weak tropical cells in the basin.

3.5. The Role of the Physical and Biological Pumps

The dominant component in the solubility pump (see section 2.1) is saturation carbon, C_{sat} . Therefore, the associated streamfunction $\Psi(\phi, C_{sat})$ (Figure 5) gives a good first approximation of the role of the solubility pump in the ocean carbon transport. There is a striking similarity with the density-latitude streamfunction (shown in, e.g., Ballarotta et al., 2014), which can be explained by the strong control that temperature exerts on C_{sat} (Weiss, 1974) and density.

It is not surprising to find many similarities between $\Psi(\phi, C_{sat})$ and $\Psi(\phi, C_{tot})$, as C_{sat} is the largest contributor to the total carbon in the ocean (Williams & Follows, 2011). The global streamfunction is characterized by three main cells. Similar to $\Psi(\phi, C_{tot})$, we can distinguish the two surface tropical cells and the surface cell in the Southern Ocean; however, the Southern Ocean cell is directly connected to the northern tropical cell. An analog to the deep anticlockwise cell can be found in $\Psi(\phi, C_{sat})$ confined to a much narrower C_{sat} concentration around 2,200 mmol m⁻³. Interestingly, the deep clockwise cell found in $\Psi(\phi, C_{tot})$ is not found in $\Psi(\phi, C_{sat})$. This will be discussed further below.

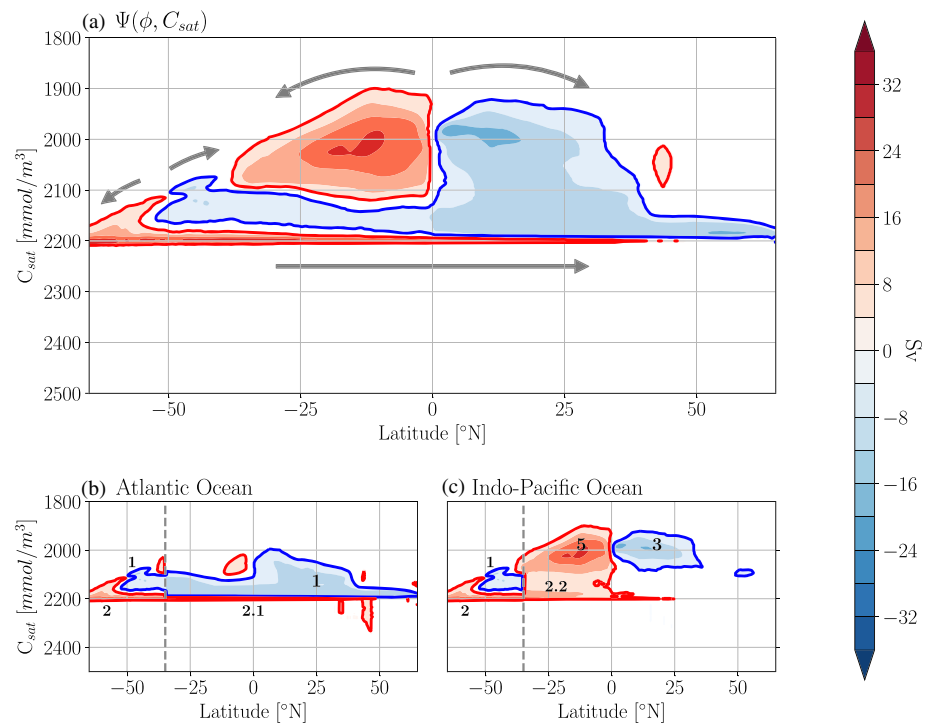


Figure 5. Upper panel: the global C_{sat} -latitude streamfunction. The lower panels represent the split of the global streamfunction into the Atlantic basin (which includes the Arctic Ocean) and the Indo-Pacific Ocean. The gray dashed line represents the cape Agulhas latitude. The C_{sat} axes has been reversed so that the tracer acts as a pseudo-depth, where the low values are found near the surface and the higher values at deeper depths. The red (blue) cells represent counterclockwise (clockwise) circulations.

The different circulation patterns of the Atlantic and the Indo-Pacific basin are captured by $\Psi(\phi, C_{sat})$. By splitting the streamfunction into separate basins, we facilitate the identification of the different circulation patterns, and their role in the oceanic carbon cycle, compared to the global streamfunction (see Figure 5). The cells in the Atlantic ocean play the same role as in $\Psi(\phi, C_{tot})$, where Cell 1 represents the AMOC and Cell 2.1 the bottom waters (Figure 5b). In the Indo-Pacific, the tropical cells (Cells 5 and 3), and the Intermediate waters (Cell 2.2) are captured by $\Psi(\phi, C_{sat})$. The reprojection of the cells into geographical space (Figures 6a and 6b) confirms that the cells in $\Psi(\phi, C_{sat})$ are a projection in the carbon space of the meridional overturning circulations in both basins (see Figure 2).

The global transport of C_{sat} is dominated by the Indo-Pacific basin, especially in the Southern Hemisphere, with a maximum equatorward transport of 1.1 Pg C yr^{-1} (Figure 6). The surface tropical cells control most of the meridional transport in the Indo-Pacific ocean. In the Atlantic, the cell linked to the AMOC carries carbon southward with a maximum value of $0.56 \text{ Pg C yr}^{-1}$ at 18°N . This cell transports a larger amount of C_{sat} than C_{tot} . This is a consequence of the undersaturation of the waters that descend in the North Atlantic to form NADW (Eggleston & Galbraith, 2018), which results in a transport of C_{dis} .

The most striking difference in the Indo-Pacific streamfunction for C_{sat} compared to C_{tot} is that it does not capture Cell 4. This suggests that the solubility pump is not responsible for the transport that occurs in this cell. The residual between the transport of C_{tot} and C_{sat} ($C_{bio+res}$; see Equation 2) represents transport of the inorganic carbon in the ocean resulting from mainly biochemical processes. There is also a contribution from the disequilibrium term and the anthropogenic carbon. $C_{bio+res}$ is not a conservative tracer as C_{bio} has internal sources and sinks. Therefore, the associated streamfunction $\Psi(\phi, C_{bio+res})$ is less straightforward to interpret.

Biological and disequilibrium processes are highly important for air-sea gas exchange (Sarmiento & Gruber, 2006). However, when studying Figures 4 and 6 and Table 1, it becomes clear that $C_{bio+res}$ contributes to a relatively small part of the total carbon transport in all cells. The only exception is Cell 4, which solely transports $C_{bio+res}$. From Figure S11 in the supporting information, we see that the $C_{bio+res}$ in this deep cell

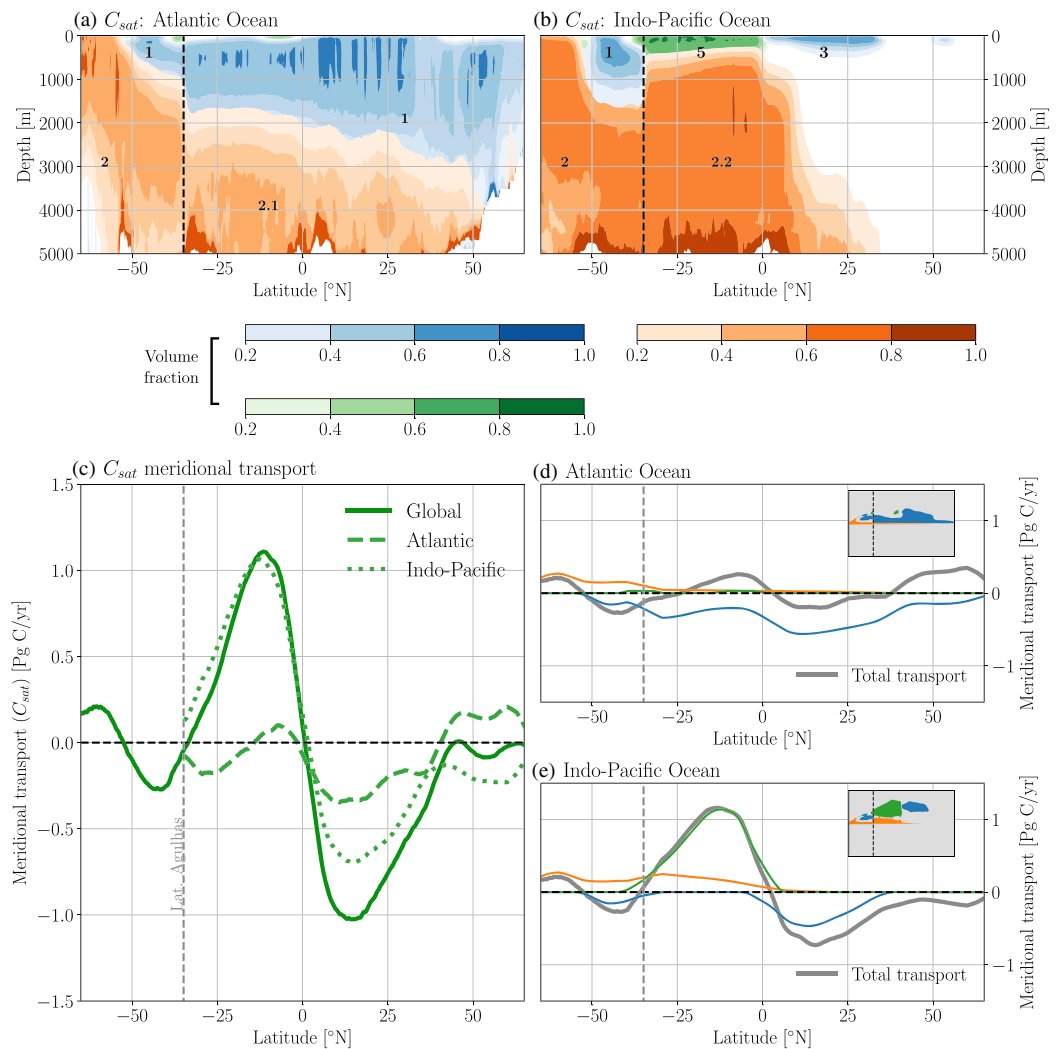


Figure 6. The identification of different cells for $\Psi(\phi, C_{sat})$ in geographical space for the Atlantic (a) and the Indo-Pacific (b) basins. The contours represent the fraction of volume at a given latitude and depth contained in the selected cell. Darker colors indicate higher fractions. (c) The global meridional transport of C_{sat} and the contribution of the different basins. The contribution of each of the cells in $\Psi(\phi, C_{sat})$ to the meridional transport for the Atlantic (d) and the Indo-Pacific basin (e). Each of the cells has an assigned color which is used for both the transport and the reprojection plots. The transports for the cells have been computed using a threshold of 4 Sv.

comes mostly from the biological pump and contains little anthropogenic or disequilibrium carbon. This suggests that the biological pump allows for carbon storage in the shadow zone (section 3.3), while the solubility pump is inefficient.

3.6. Carbon Budget and Eddy-Driven Transport

The aim of this section is to present a budget (Figure 7) showing the carbon transport between different regions of the global ocean together with the local air-sea CO_2 exchange and accumulation and to give an estimate of the eddy-driven transport. Due to mass conservation, the transport of inorganic carbon by the ocean circulation has to match boundary fluxes, accumulation, eddy-driven transport, and transport of organic carbon. The eddy-driven transport is not captured in our data because of the coarse time-resolution, but it can be computed knowing all other fluxes. Because of the constant forcing of anthropogenic carbon, the ocean carbon system is not in steady state, and there is a net accumulation of $1.73 \text{ Pg C yr}^{-1}$ of anthropogenic carbon. Boundary fluxes include air-sea CO_2 exchange and sediment-water C exchange. The net sediment CO_2 fluxes, as well as the meridional transport of organic carbon, in our model are negligible, and we therefore leave them out.

Table 1

Maximum Carbon Transport for Each of the Cells in Pg C yr^{-1}

Cell	basin	C_{tot} (mean)	C_{tot} (max)	C_{sat} (mean)	C_{sat} (max)	Primary association
1	Atlantic	−0.13	−0.44	−0.19	−0.56	AMOC
2.1	Atlantic	0.10	0.37	0.08	0.27	Intermediate waters/AABW
2.2	Indo-Pacific	0.12	0.37	0.12	0.27	Intermediate waters
3	Indo-Pacific	−0.25	−0.58	−0.22	−0.47	ST Gyre
4	Indo-Pacific	−0.14	−0.35	–	–	Deep/Bottom Water
5	Indo-Pacific	0.44	1.42	0.36	1.14	ST Gyre

The top part of Figure 7 shows the net air-sea CO_2 fluxes. There is a net uptake of carbon in all the regions except in the tropical one where there is a net outgassing. The red bars represent the standard deviation of those fluxes showing high variability in the temperate regions in both hemispheres. This large variability is a result of the seasonal changes in temperature and primary production that impact the ocean carbon uptake. The net uptake of carbon in this study is $1.73 \text{ Pg C yr}^{-1}$. The flux distribution and the net uptake value are in good correspondence with values found in literature (Gruber et al., 2009; Mikaloff Fletcher et al., 2007).

The next set of bars represents the meridional carbon transport of C_{tot} , C_{sat} , and $C_{bio+res}$ at given latitudes. $C_{bio+res}$ includes all terms not represented by C_{sat} . As described in section 3.5, the transport of C_{sat} is the major contributor to the total meridional transport of carbon. However, in the high-latitude Northern Hemisphere, $C_{bio+res}$ is dominant in the total transport. Below the transport bars, the accumulation of carbon in each region is shown. The tropics are the region with the largest accumulation rate ($0.69 \text{ Pg C yr}^{-1}$) followed by the south-hemispheric temperate region ($0.54 \text{ Pg C yr}^{-1}$). The Northern Hemisphere, especially at high latitudes, showed the lowest accumulation rates.

The accumulation in each of the regions and the convergence/divergence of carbon transports are not enough to close the carbon budget. Therefore, the discrepancy terms are shown in the last panel. These discrepancies are computed by closing the carbon budget at each of the latitudinal regions starting from the Southern Ocean. The dominant contributors to these discrepancies are likely to be the effect of diffusivity and the frequency of the output data. As our data are output with a monthly frequency, we do not capture the carbon transports advected by eddies at smaller time scales.

Transport convergences and CO_2 fluxes

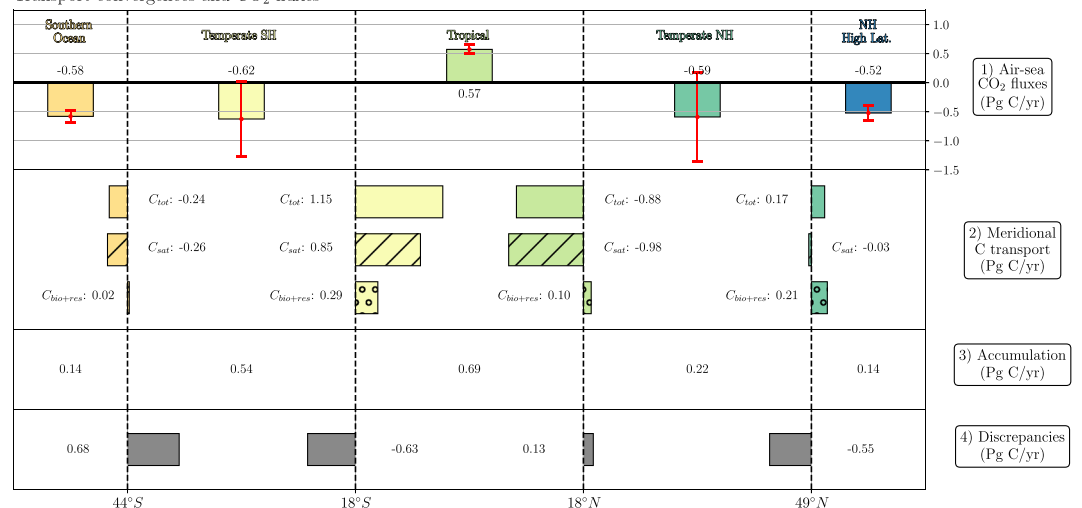


Figure 7. Carbon budget in the ocean for different regions. Upper panel: integrated CO_2 surface fluxes for different regions; the red error bars represent the standard deviation of the fluxes. The meridional transports of C_{tot} at given latitudes and the contribution of the different components are represented in the second panel. The accumulation of carbon as a result of the anthropogenic carbon are shown in the third panel. The last row represents the discrepancy terms required to close the budget. Units are given in Pg C yr^{-1} .

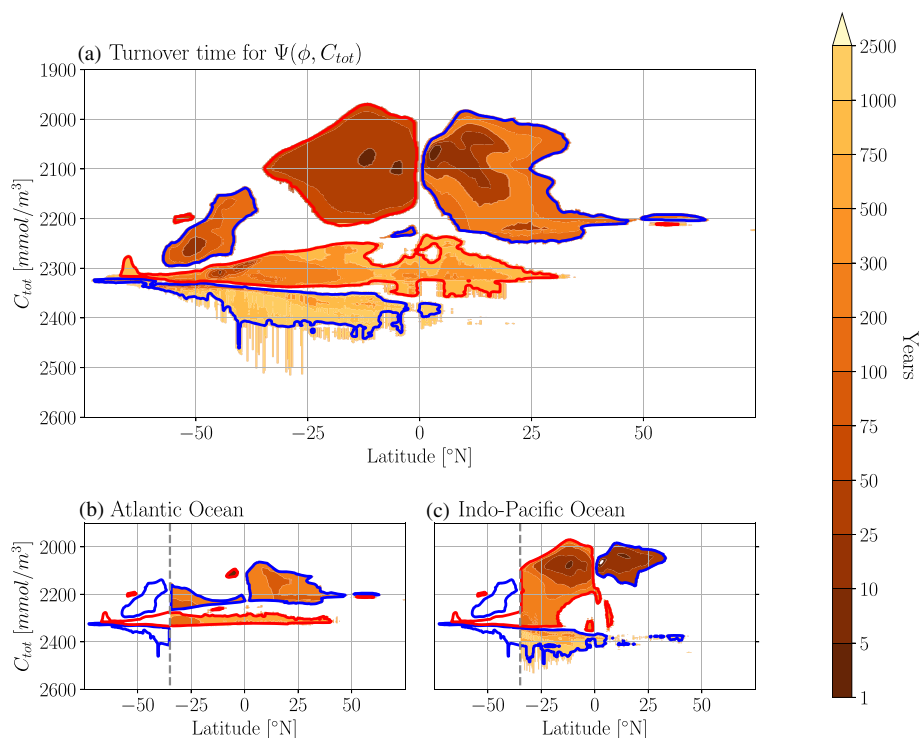


Figure 8. The turnover times computed from $\Psi(\phi, C_{tot})$ for the global case (a) and for the two basins: Atlantic (b) and Indo-Pacific (c). The streamline interval has been chosen to 4 Sv. Units given in years.

4. Turnover Time

More information on the role of the circulation cells in keeping CO_2 from the atmosphere is obtained when looking at their turnover times. The turnover time, τ , gives an estimate of how much time is required for the entire volume contained between two streamlines to complete a cycle in the cell. That is,

$$\tau = \frac{\Delta V}{\Delta \Psi}, \quad (7)$$

where $\Delta \Psi$ represents the selected streamlines and ΔV is the volume contained in between those streamlines. The turnover times for $\Psi(\phi, C_{tot})$ are presented in Figure 8; we have selected intervals of 4 Sv between streamlines.

The near-surface cells have short turnover times of the order of decades; this result is not surprising as these cells are both the strongest and are confined in a small volume. The decomposition of the streamfunction shows that the tropical cells in the Indo-Pacific Ocean are those with the shortest turnover times (<50 years), followed by the AMOC cell (around 100–300 years) and the bottom cell in the Atlantic (300–500 years). The longest time scales, on the order of more than 1,000 years, are associated with the deep cell in the Indo-Pacific Ocean. As this cell only consists of C_{bio} , it indicates that the biological pump in the Indo-Pacific is the most important process for storing CO_2 from the atmosphere on longer time scales.

5. Conclusions

As the largest dynamic reservoir of carbon in the Earth system, the ocean plays an important role in influencing climate. However, understanding its carbon cycle is complicated by the diverse roles played by its water masses, circulation, and biogeochemical processes, and separating these processes in observational data or model output using traditional methods is difficult. In this study, we show how to apply latitude-tracer streamfunctions, a diagnostic tool well-known in physical oceanography to facilitate the understanding of processes in the ocean. We have chosen to focus on the ocean's dissolved inorganic carbon pool as this buffers the atmospheric concentration of CO_2 that has an important role in climate.

This diagnostic tool connects a commonly used framework for understanding of the ocean circulation (streamfunctions) with a commonly used framework for understanding the ocean carbon cycle and its sources and sinks (carbon separation). This way, we are able to separate the roles played by different water masses and circulation pathways on the carbon cycle. We find that the shallow subtropical gyres are the main contributor to meridional carbon transport in the ocean, carrying carbon from the midlatitudes into the equatorial region. According to our model, they transport up to $1.42 \text{ Pg C yr}^{-1}$, while the overturning represented by deeper water masses such as the AABW and PDW only carry up to $0.35 \text{ Pg C yr}^{-1}$. By separating the carbon into its different constituents, we are additionally able to show that the carbon transported in the subtropical cells and the deep Atlantic mainly originates from the the solubility pump and thus air-sea exchange of CO_2 , while the carbon transport in the deep Pacific is mainly of biogenic origin.

For the studies of future climate variability and CO_2 uptake by the ocean, this method can simplify model intercomparisons and allow us to put error bars on the role of different water masses in future ocean carbon uptake/release. It will allow us to identify notable changes in ocean carbon transport and identify the responsible processes. A further advantage of this streamfunction methodology is the possibility of computing the turnover time of each of the cells. Insights gained from studying turnover time can be helpful in understanding changes in ocean carbon transport across climate states (e.g., glacial-interglacial cycles). In this way, this tool can advance, and provide more detail to, the understanding of the oceans role in carbon sequestration.

Appendix A: Discretization of the Streamfunction

We will here explain how we computed $\Psi(\phi, \xi)$ by numerical discretization of Equation 4, using finite differences. Let us consider a gridded 3D field for the total meridional velocity $v_{i,j,k,n}$ and the tracer field $\xi_{i,j,k,n}$, where i, j, k represent the spatial indexes and n represents the time index. Moreover, we will define a discretized space of the tracer ξ_m^D as a function of the index m , so that $\xi_m^D = \xi_{min}^D + (m - 1)\Delta\xi$.

The streamfunction in the discrete form can be written as

$$\psi_{j,m} = \frac{1}{N} \sum_{n=1}^N \sum_{i=1}^I \sum_{k=1}^K v_{i,j,k,n} \mu[m - l_{i,j,k,n}] \Delta z_{i,j,k} \Delta x_{i,j}, \quad (\text{A1})$$

where N is the total number of time steps consider and I and K are the maximum value of the zonal and vertical indexes. Besides, $\mu[*]$ is the discrete unit function where $l_{i,j,k,n}$ is the index corresponding to the nearest ξ_l^D for $\xi_{i,j,k,n}$ ($l_{i,j,k,n} = 1 + \lfloor \frac{\xi_{i,j,k,n} - \xi_{min}^D}{\Delta\xi} + 0.5 \rfloor$).

Appendix B: A Note About Discretization

The meridional tracer transport can be computed directly by integrating the streamfunction in the continuous form. However, this direct relationship does not hold directly in the discrete form. There are two main sources of error in the computation: the resolution of the binning space and the choice of the minimum and maximum value of the range.

The discrete version of the meridional transport computed directly from the velocity and the tracer fields is given by the following equation:

$$Tr_j^{(1)} = \frac{1}{N} \sum_{n=1}^N \sum_{i=1}^I \sum_{k=1}^K v_{i,j,k,n} (\xi_{i,j,k,n} - \xi_{ref}) \Delta z_{i,j,k} \Delta x_{i,j}. \quad (\text{B1})$$

Similarly, the discrete version of the meridional tracer transport computed from the streamfunction (Equation 5) is given by

$$Tr_j^{(2)} = \sum_{m=1}^{M-1} (\xi_m^D - \xi_{ref}) \frac{\psi_{j,m+1} - \psi_{j,m}}{\Delta\xi} \Delta\xi = \sum_{m=1}^{M-1} (\xi_m^D - \xi_{ref}) (\psi_{j,m+1} - \psi_{j,m}). \quad (\text{B2})$$

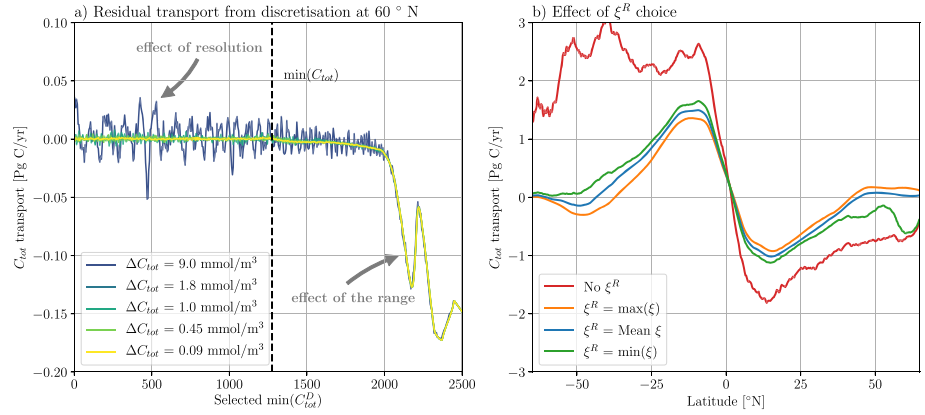


Figure B1. (a) The residual transport at 60°N as a result of the discretization. The solid color lines represent different resolutions of the discretized tracer space. If the selected range includes all the possible values of the tracer, the residual transport depends only on the resolution. The minimum value of C_{tot} is represented by the dashed line. (b) The global transport for C_{tot} for different choices for ξ^R . A right choice of this value will minimize the effect of divergence. If the system would be nondivergent, the results for the transport would become insensitive to the choice of ξ^R .

Inserting the definition of the discretized streamfunction (Equation A1), we can obtain the following expression for the discretized transport:

$$\begin{aligned} Tr_j^{(2)} &= \frac{1}{N} \sum_{n=1}^N \sum_{i=1}^I \sum_{k=1}^K v_{i,j,k,n} \left(\sum_{m=1}^{M-1} (\xi_m^D - \xi_{ref}) \delta[m - l_{i,j,k,n}] \right) \Delta z_{i,j,k} \Delta x_{i,j} = \\ &= \frac{1}{N} \sum_{n=1}^N \sum_{i=1}^I \sum_{k=1}^K v_{i,j,k,n} (\xi_{i,j,k,n}^D - \xi_{ref}) \Delta z_{i,j,k} \Delta x_{i,j}. \end{aligned} \quad (B3)$$

In contrast to Equation B1, the tracer field in this case is given by the nearest value in the discrete space.

We will denote as the residual transport, ϵ , the difference between the transport computed directly and the one computed from the streamfunction:

$$\begin{aligned} \epsilon &\equiv Tr_j^{(1)} - Tr_j^{(2)} = \frac{1}{N} \sum_{n=1}^N \sum_{i=1}^I \sum_{k=1}^K v_{i,j,k,n} (\xi_{i,j,k,n} - \xi_{i,j,k,n}^D) \Delta z_{i,j,k} \Delta x_{i,j} \\ &= \frac{1}{N} \sum_{n=1}^N \sum_{i=1}^I \sum_{k=1}^K v_{i,j,k,n} \delta \xi_{i,j,k,n} \Delta z_{i,j,k} \Delta x_{i,j}, \end{aligned} \quad (B4)$$

where $\delta \xi_{i,j,k,n}$ represents the difference between the original and the nearest value in the discrete space of the tracer. This term is bounded by the resolution of the tracer $\Delta \xi$,

$$\epsilon = |\mathcal{O}(\delta \xi_{i,j,k,n})| \leq \mathcal{O}(\Delta \xi). \quad (B5)$$

A coarse resolution in the binning will have as a result an overestimation or a subestimation of the transports. This residual transport will decrease in a finer resolution.

The selected range for the tracer is also important. The range should include all the possible values of the tracer. If a value of the tracer is outside the range, the transport associated to that water mass will be miscalculated. This error can be reduced by selecting a range that covers all the possible values of the tracer. In Figure B1a, we represent the residual transport at 60°N for different resolutions and minimum values of the tracer in the discrete form. In all the cases, the maximum value of tracer is kept constant. If our discrete space includes all the possible values of the tracer, the residual transport is a result of the discretization. The resolution used in this study ($\Delta C_{tot} = 1.0 \text{ mmol m}^{-3}$) is fine enough to obtain a negligible residual transport. The effect of the selected range has a significant impact as our domain includes fewer of the possible values of the tracer. This residual transport is independent of the chosen resolution.

Another important factor is the choice of the reference tracer value, ξ^R , when computing the meridional transport. The computed transports are sensitive to this choice in regions with large volume transports (here,

the Southern Ocean; see Figure B1b). By using the mean value rather than the minimum or maximum, our computed transports provide a plausible estimate between the two extremes.

Data Availability Statement

Fortran codes used for the data analysis and computation of the streamfunctions in section 2.2 are available from GitHub (<https://doi.org/10.5281/zenodo.3256350>). Relevant model output data, streamfunctions, and the meridional transports computed in this study are available from Zenodo (<https://doi.org/10.5281/zenodo.3254449>).

Acknowledgments

This work has been financially supported by the Bolin Centre for Climate Research. F.F. wants to acknowledge Bolin Center for Climate Research, research areas 1 (Oceans – atmosphere dynamics and climate) and 4 (Biogeochemical cycles and climate), for funding. SG acknowledge support from the Australian Research Council Grant FL150100090. The modeling component of this work used the ARCHER UK National Supercomputing Service (<http://www.archer.ac.uk>) and was primarily supported by NERC National Capability funding and the Regional Ocean Modelling project (ROAM; grant NE/H017372/1). The analysis and storage of data were performed on resources provided by the Swedish National Infrastructure for Computing (SNIC) at the National Centre at Linköping University (NSC). This manuscript has benefited from discussions with Kevin I. C. Oliver, Gurvan Madec, Casimir de Lavergne, and David Ferreira, and the authors would like to thank them for their useful comments. The authors also would like to thank the two anonymous reviewers that substantially improved the manuscript.

References

- Ballarotta, M., Falahat, S., Brodeau, L., & Döös, K. (2014). On the glacial and interglacial thermohaline circulation and the associated transports of heat and freshwater. *Ocean Science*, 10(6), 907–921. <https://doi.org/10.5194/os-10-907-2014>
- Brewer, P. G., Goyet, C., & Dyrssen, D. (1989). Carbon dioxide transport by ocean currents at 25°N latitude in the Atlantic Ocean. *Science*, 246(4929), 477–479. <https://doi.org/10.1126/science.246.4929.477>
- Broecker, W. S. (1983). The ocean. *Scientific American*, 249(3), 146–161.
- Broecker, W. S., & Peng, T. H. (1992). Interhemispheric transport of carbon dioxide by ocean circulation. *Nature*, 356, 587–589. Retrieved from <http://www.nature.com/nature/journal/v356/n6370/abs/356587a0.html>
- Ciais, P., Sabine, C., Bala, G., Bopp, L., Brovkin, V., Canadell, J., et al. (2013). Carbon and other biogeochemical cycles. In T. F. Stocker et al. (Eds.), *Climate change 2013: The physical science basis. contribution of working group i to the fifth assessment report of the intergovernmental panel on climate change* (pp. 465–570). Cambridge, United Kingdom and New York, NY, USA: Cambridge University Press. <https://doi.org/10.1017/CBO9781107415324.015>
- Couldrey, M. P. (2018). Mechanisms of ocean carbon cycle variability in the 21st century (Ph.D. Thesis), University of Southampton. Retrieved from <https://eprints.soton.ac.uk/421105>
- de Lavergne, C., Madec, G., Roquet, F., Holmes, R. M., & McDougall, T. J. (2017). Abyssal ocean overturning shaped by seafloor distribution. *Nature*, 551(7679), 181–186. <https://doi.org/10.1038/nature24472>
- Döös, K., Nilsson, J., Nycander, J., Brodeau, L., & Ballarotta, M. (2012). The world ocean thermohaline circulation. *Journal of Physical Oceanography*, 42(9), 1445–1460. <https://doi.org/10.1175/JPO-D-11-0163.1>
- Döös, K., & Webb, D. J. (1994). The Deacon cell and the other meridional cells of the Southern Ocean. *Journal of Physical Oceanography*, 24(2), 429–442. [https://doi.org/10.1175/1520-0485\(1994\)024<0429:tdcato>2.0.co;2](https://doi.org/10.1175/1520-0485(1994)024<0429:tdcato>2.0.co;2)
- Eggleston, S., & Galbraith, E. D. (2018). The devil's in the disequilibrium: Multi-component analysis of dissolved carbon and oxygen changes under a broad range of forcings in a general circulation model. *Biogeosciences*, 15(12), 3761–3777. <https://doi.org/10.5194/bg-15-3761-2018>
- Gloor, M., Gruber, N., Sarmiento, J., Sabine, C. L., Feely, R. A., & Rödenbeck, C. (2003). A first estimate of present and preindustrial air-sea CO₂ flux patterns based on ocean interior carbon measurements and models. *Geophysical Research Letters*, 30(1), 1010. <https://doi.org/10.1029/2002GL015594>
- Groeskamp, S., Lenton, A., Matear, R., Sloyan, B. M., & Langlais, C. (2016). Anthropogenic carbon in the ocean—Surface to interior connections. *Global Biogeochemical Cycles*, 30, 1682–1698. <https://doi.org/10.1002/2016GB005476>
- Groeskamp, S., Zika, J. D., McDougall, T. J., Sloyan, B. M., & Laliberté, F. (2014). The representation of ocean circulation and variability in thermodynamic coordinates. *Journal of Physical Oceanography*, 44(7), 1735–1750. <https://doi.org/10.1175/JPO-D-13-0213.1>
- Gruber, N., Gloor, M., Mikaloff Fletcher, S. E., Doney, S. C., Dutkiewicz, S., Follows, M. J., et al. (2009). Oceanic sources, sinks, and transport of atmospheric CO₂. *Global Biogeochemical Cycles*, 23, GB1005. <https://doi.org/10.1029/2008GB003349>
- Ito, T., & Follows, M. J. (2005). Preformed phosphate, soft tissue pump and atmospheric CO₂. *Journal of Marine Research*, 63(4), 813–839. <https://doi.org/10.1357/0022240054663231>
- Iudicone, D., Rodgers, K. B., Stendardo, I., Aumont, O., Madec, G., Bopp, L., et al. (2011). Water masses as a unifying framework for understanding the Southern Ocean carbon cycle. *Biogeosciences*, 8(5), 1031–1052. <https://doi.org/10.5194/bg-8-1031-2011>
- Jones, C. D., Hughes, J. K., Bellouin, N., Hardiman, S. C., Jones, G. S., Knight, J., et al. (2011). The HadGEM2-ES implementation of CMIP5 centennial simulations. *Geoscientific Model Development*, 4(3), 543–570. <https://doi.org/10.5194/gmd-4-543-2011>
- Landschützer, P., Gruber, N., Haumann, F. A., Rödenbeck, C., Bakker, D. C. E., van Heuven, S., et al. (2015). The reinvigoration of the Southern Ocean carbon sink. *Science*, 349(6253), 1221–1224. <https://doi.org/10.1126/science.aab2620>
- Lauderdale, J. M., Garabato, A. C. N., Oliver, K. I. C., Follows, M. J., & Williams, R. G. (2013). Wind-driven changes in Southern Ocean residual circulation, ocean carbon reservoirs and atmospheric CO₂. *Climate Dynamics*, 41(7–8), 2145–2164.
- Le Quéré, C., Rödenbeck, C., Buitenhuis, E. T., Conway, T. J., Langenfelds, R., Gomez, A., et al. (2007). Saturation of the Southern Ocean CO₂ sink due to recent climate change. *Science*, 316(5832), 1735–1738. <https://doi.org/10.1126/science.1136188>
- Levy, M., Bopp, L., Karleskind, P., Resplandy, L., Etche, C., & Pinsard, F. (2013). Physical pathways for carbon transfers between the surface mixed layer and the ocean interior. *Global Biogeochemical Cycles*, 27, 1001–1012. <https://doi.org/10.1002/gbc.20092>
- Lewis, E., Wallace, D., & Allison, L. J. (1998). Program developed for CO₂ system calculations (ORNL/CDIAC-105): Carbon Dioxide Information Analysis Center, managed by Lockheed Martin Energy Research Corporation for the US Department of Energy Tennessee.
- Madec, G. (2012). NEMO ocean engine. *Note du Pôle de modélisation, Institut Pierre-Simon Laplace (IPSL)* (Vol. 27, p. 357). Retrieved from <http://eprints.soton.ac.uk/64324/>
- Marshall, J., & Speer, K. (2012). Closure of the meridional overturning circulation through Southern Ocean upwelling. *Nature Geoscience*, 5(3), 171–180. <https://doi.org/10.1038/ngeo1391>
- McDougall, T. J., & Barker, P. M. (2011). Getting started with TEOS-10 and the Gibbs Seawater (GSW) oceanographic toolbox. *SCOR/IAPSO WG*, 127, 1–28.
- Mikaloff Fletcher, S. E., Gruber, N., Jacobson, A. R., Gloor, M., Doney, S. C., Dutkiewicz, S., et al. (2007). Inverse estimates of the oceanic sources and sinks of natural CO₂ and the implied oceanic carbon transport. *Global Biogeochemical Cycles*, 21, GB1010. <https://doi.org/10.1029/2006GB002751>
- Ödalen, M., Nycander, J., Oliver, K. I. C., Brodeau, L., & Ridgwell, A. (2018). The influence of the ocean circulation state on ocean carbon storage and CO₂ drawdown potential in an Earth system model. *Biogeosciences*, 15, 1367–1393. <https://doi.org/10.5194/bg-15-1367-2018>

- Raven, J. A., & Falkowski, P. G. (1999). Oceanic sinks for atmospheric CO₂. *Plant, Cell & Environment*, 22(6), 741–755.
- Sabine, C. L., Feely, R. A., Gruber, N., Key, R. M., Lee, K., Bullister, J. L., et al. (2004). The oceanic sink for anthropogenic CO₂. *Science*, 305(5682), 367–371. <https://doi.org/10.1126/science.1097403>
- Sarmiento, J. L., & Gruber, N. (2006). *Ocean biogeochemical dynamics*. Princeton, Woodstock: Princeton University Press.
- Speer, K., Rintoul, S. R., & Sloyan, B. (2000). The Diabatic Deacon Cell* *Journal of Physical Oceanography*, 30(12), 3212–3222. [https://doi.org/10.1175/1520-0485\(2000\)030h3212:TDDCi2.0.CO;2](https://doi.org/10.1175/1520-0485(2000)030h3212:TDDCi2.0.CO;2)
- Takahashi, T., Sutherland, S. C., Sweeney, C., Poisson, A., Metzl, N., Tilbrook, B., et al. (2002). Global sea–air CO₂ flux based on climatological surface ocean pCO₂, and seasonal biological and temperature effects. *Deep Sea Research Part II: Topical Studies in Oceanography*, 49(9–10), 1601–1622. [https://doi.org/10.1016/S0967-0645\(02\)00003-6](https://doi.org/10.1016/S0967-0645(02)00003-6)
- Talley, L. D. (2013). Closure of the global overturning circulation through the Indian, Pacific, and Southern Oceans: Schematics and transports. *Oceanography*, 26, 80–97. <https://doi.org/10.5670/oceanog.2013.07>
- Timmermann, R., Goosse, H., Madec, G., Fichefet, T., Ethe, C., & Dulière, V. (2005). On the representation of high latitude processes in the ORCA-LIM global coupled sea ice-ocean model. *Ocean Modelling*, 8(1–2), 175–201. <https://doi.org/10.1016/j.ocemod.2003.12.009>
- Volk, T., & Hoffert, M. I. (1985). Ocean carbon pumps: Analysis of relative strengths and efficiencies in ocean-driven atmospheric CO₂ changes. In E. T. Sundquist & W. S. Broecker (Eds.), *The carbon cycle and atmospheric CO: Natural variations Archean to present* (pp. 99–110). Washington, DC: American Geophysical Union.
- Volk, T., & Hoffert, M. I. (2013). Ocean carbon pumps: Analysis of relative strengths and efficiencies in ocean-driven atmospheric CO₂ changes. In *The carbon cycle and atmospheric CO₂: Natural variations Archean to present* (pp. 99–110). Washington, DC: American Geophysical Union. <https://doi.org/10.1029/GM032p0099>
- Weiss, R. (1974). Carbon dioxide in water and seawater: The solubility of a non-ideal gas. *Marine chemistry*, 2(3), 203–215.
- Williams, R. G., & Follows, M. J. (2011). *Ocean dynamics and the carbon cycle: Principles and mechanisms*. Cambridge: Cambridge University Press. <https://doi.org/10.1017/CBO9780511977817>
- Yasunaka, S., Siswanto, E., Olsen, A., Hoppema, M., Watanabe, E., Fransson, A., et al. (2018). Arctic Ocean CO₂ uptake: An improved multiyear estimate of the air–sea CO₂ flux incorporating chlorophyll *a* concentrations. *Biogeosciences*, 15(6), 1643–1661. <https://doi.org/10.5194/bg-15-1643-2018>
- Yool, A., Popova, E. E., & Anderson, T. R. (2013). MEDUSA-2.0: An intermediate complexity biogeochemical model of the marine carbon cycle for climate change and ocean acidification studies. *Geoscientific Model Development*, 6(5), 1767–1811. <https://doi.org/10.5194/gmd-6-1767-2013>
- Yool, A., Popova, E. E., & Coward, A. C. (2015). Future change in ocean productivity : Is the Arctic the new Atlantic? *Journal of Geophysical Research: Oceans*, 120, 7771–7790. <https://doi.org/10.1002/2015JC011167>
- Zika, J. D., England, M. H., & Sijp, W. P. (2012). The ocean circulation in thermohaline coordinates. *Journal of Physical Oceanography*, 42(5), 708–724. <https://doi.org/10.1175/JPO-D-11-0139.1>